

# X-ray phase contrast microscopy at 300 nm resolution with laboratory sources

Daniele Pelliccia,<sup>1,\*</sup> Andrea Sorrentino,<sup>2</sup> Inna Bukreeva,<sup>2,3</sup> Alessia Cedola,<sup>2</sup> Fernando Scarinci,<sup>2</sup> Mihaela Ilie,<sup>2</sup> Anna Maria Gerardino,<sup>2</sup> Michela Fratini,<sup>2</sup> and Stefano Lagomarsino<sup>2</sup>

<sup>1</sup>*School of Physics, Monash University, Clayton, Victoria 3800, Australia*

<sup>2</sup>*Istituto di Fotonica e Nanotecnologie (IFN), Consiglio Nazionale delle Ricerche, Via Cineto Romano 42,00156 Roma, Italy*

<sup>3</sup>*Russian Academy of Science, P. N. Lebedev Physics Institute, Leninsky pr. 53, 119991 Moscow, Russia*  
\*[daniele.pelliccia@sci.monash.edu.au](mailto:daniele.pelliccia@sci.monash.edu.au)

**Abstract:** We report the performance of an X-ray phase contrast microscope for laboratory sources with 300 nm spatial resolution. The microscope is based on a commercial X-ray microfocus source equipped with a planar X-ray waveguide able to produce a sub-micrometer x-ray beam in one dimension. Phase contrast images of representative samples are reported. The achieved contrast and resolution is discussed for different configurations. The proposed approach could represent a simple, inexpensive, solution for sub-micrometer resolution imaging with small laboratory setups.

©2010 Optical Society of America

**OCIS codes:** (340.0340) X-ray optics; (340.7460) X-ray microscopy; (340.7440) X-ray imaging.

---

## References and links

1. U. Bonse, and M. Hart, "An x-ray interferometer," *Appl. Phys. Lett.* **6**(8), 155–156 (1965).
2. A. Momose, "Phase-contrast X-ray imaging based on interferometry," *J. Synchrotron Radiat.* **9**(3), 136–142 (2002).
3. C. David, B. Nöhhammer, H. H. Solak, and E. Ziegler, "Differential x-ray phase contrast imaging using a shearing interferometer," *Appl. Phys. Lett.* **81**(17), 3287–3289 (2002).
4. D. Chapman, W. Thomlinson, R. E. Johnston, D. Washburn, E. Pisano, N. Gmür, Z. Zhong, R. Menk, F. Arfelli, and D. Sayers, "Diffraction enhanced x-ray imaging," *Phys. Med. Biol.* **42**(11), 2015–2025 (1997).
5. P. Cloetens, R. Barrett, J. Baruchel, J.-P. Guigay, and M. Schlenker, "Phase objects in synchrotron radiation hard x-ray imaging," *J. Phys. D Appl. Phys.* **29**(1), 133–146 (1996).
6. K. A. Nugent, T. E. Gureyev, D. J. Cookson, D. Paganin, and Z. Barnea, "Quantitative phase imaging using hard x-rays," *Phys. Rev. Lett.* **77**(14), 2961–2964 (1996).
7. A. Pogany, D. Gao, and S. W. Wilkins, "Contrast and resolution in imaging with a microfocus x-ray source," *Rev. Sci. Instrum.* **68**(7), 2774–2782 (1997).
8. S. V. Gasilov, A. Ya. Faenov, T. A. Pikuz, Y. Fukuda, M. Kando, T. Kawachi, I. Yu. Skobelev, H. Daido, Y. Kato, and S. V. Bulanov, "Wide-field-of-view phase-contrast imaging of nanostructures with a comparatively large polychromatic soft x-ray plasma source," *Opt. Lett.* **34**(21), 3268–3270 (2009).
9. S. Almaviva, F. Bonfigli, I. Franzini, A. Lai, R. M. Montereali, D. Pelliccia, A. Cedola, and S. Lagomarsino, "Hard x-ray contact microscopy with 250 nm spatial resolution using a LiF film detector and a tabletop microsource," *Appl. Phys. Lett.* **89**(5), 054102 (2006).
10. R. Toth, J. C. Kieffer, S. Fourmaux, T. Ozaki, and A. Krol, "In-line phase-contrast imaging with a laser-based hard x-ray source," *Rev. Sci. Instrum.* **76**(8), 083701 (2005).
11. S. C. Mayo, P. R. Miller, S. W. Wilkins, T. J. Davis, D. Gao, T. E. Gureyev, D. Paganin, D. J. Parry, A. Pogany, and A. W. Stevenson, "Quantitative X-ray projection microscopy: phase-contrast and multi-spectral imaging," *J. Microsc.* **207**(2), 79–96 (2002).
12. S. C. Mayo, T. J. Davis, T. E. Gureyev, P. R. Miller, D. Paganin, A. Pogany, A. W. Stevenson, and S. W. Wilkins, "X-ray phase-contrast microscopy and microtomography," *Opt. Express* **11**(19), 2289–2302 (2003).
13. S. Lagomarsino, W. Jark, S. Di Fonzo, A. Cedola, B. Mueller, P. Engstrom, and C. Riekkel, "Sub-micro-meter X-ray beam production by a thin film wave-guide," *J. Appl. Phys.* **79**(8), 4471–4473 (1996).
14. W. Jark, S. Di Fonzo, S. Lagomarsino, A. Cedola, E. di Fabrizio, A. Bram, and C. Riekkel, "Properties of a submicrometer x-ray beam at the exit of a waveguide," *J. Appl. Phys.* **80**(9), 4831–4836 (1996).
15. D. Pelliccia, I. Bukreeva, M. Ilie, W. Jark, A. Cedola, F. Scarinci, and S. Lagomarsino, "Computer simulations and experimental results on air-gap X-ray waveguides," *Spectrochim. Acta, B At. Spectrosc.* **62**(6-7), 615–621 (2007).

16. L. De Caro, C. Giannini, S. Di Fonzo, W. Jark, A. Cedola, and S. Lagomarsino, "Spatial coherence of x-ray planar waveguide exiting radiation," *Opt. Commun.* **217**(1-6), 31–45 (2003).
  17. L. De Caro, A. Cedola, C. Giannini, I. Bukreeva, and S. Lagomarsino, "In-line phase-contrast imaging for strong absorbing objects," *Phys. Med. Biol.* **53**(22), 6619–6637 (2008).
  18. I. Bukreeva, D. Pelliccia, A. Cedola, F. Scarinci, M. Ilie, C. Giannini, L. De Caro, and S. Lagomarsino, "Analysis of tapered front-coupling X-ray waveguides," *J. Synchrotron Radiat.* **17**(1), 61–68 (2010).
  19. M. Born, and E. Wolf, *Principles of Optics* (Pergamon Press, Oxford, 1986).
  20. S. Di Fonzo, W. Jark, S. Lagomarsino, C. Giannini, L. De Caro, A. Cedola, and M. Müller, "Non-destructive determination of local strain with 100-nanometre spatial resolution," *Nature* **403**(6770), 638–640 (2000).
  21. L. De Caro, C. Giannini, D. Pelliccia, C. Mocuta, T. H. Metzger, A. Guagliardi, A. Cedola, I. Burkeeva, and S. Lagomarsino, "In-line holography and coherent diffractive imaging with x-ray waveguides," *Phys. Rev. B* **77**(8), 081408 (2008).
  22. F. Pfeiffer, C. David, M. Burghammer, C. Riekel, and T. Salditt, "Two-dimensional x-ray waveguides and point sources," *Science* **297**(5579), 230–234 (2002).
- 

## 1. Introduction

X-ray phase contrast is nowadays an established technique to image low absorbing samples nondestructively. In the x-ray spectral region, the index of refraction is written as  $n = 1 - \delta - i\beta$ , where the real and imaginary parts account respectively for phase shifting and absorption of the incident wave. In the hard x-ray spectral range it is  $\delta \gg \beta$ , thus the phase shift effect is much stronger than the absorption. Several techniques have been proposed so far to transfer the phase modulations into detectable intensity modulations. Without the sake of completeness, we can mention on one hand, the interferometer techniques with crystals [1,2], with gratings [3] and the analyzer-based techniques such as the Diffraction Enhanced Imaging [4]. Such techniques usually exhibit high phase sensitivity but they require high x-ray flux and/or high transverse coherence and monochromaticity to give sufficient signal-to-noise ratio in the acquired images.

On the other hand, the propagation-based techniques [5–7] are usually less sensitive to slight phase gradients but they can be performed with simpler experimental setup, and they can be scaled down from synchrotron sources to laboratory sources. The main effects contributing to the achievable contrast and the resolution in propagation-based phase contrast imaging are the degree of coherence of the incoming beam (related to the source size and the distance source-sample) and the detector resolution [7]. Therefore phase contrast x-ray imaging in propagation is well performed with synchrotron radiation where a relatively small source size (tens microns) is combined with large propagation distances (tens meters) to create a nearly parallel illumination of the sample with high coherence length. In this way the achievable contrast is usually large and it can be detected with high resolution detectors, placed downstream. Namely this approach has been used also in laboratory-based setups (with much smaller propagation distances) equipped with high resolution detector based on LiF (Lithium Fluoride) films [8,9]. Such method can obtain high resolution, wide field of view, imaging, but the detection efficiency is limited to soft x-rays [8] for phase contrast applications, or hard x-rays [9] for absorption contrast imaging. In addition the read-out process of the LiF films *via* an optical microscope, limits the applicability of the technique to off-line experiments.

Alternatively, if the source size can be made small enough, a sufficient coherent illumination is achieved also with shorter propagation distances, thus allowing one to scale the setup to smaller laboratory sources, with no stringent demand on the detector resolution. In fact, since the source provides a divergent beam, an effective magnification of the sample image on the detector screen is implemented. This permits the use of detectors with moderate resolution (thus increasing the detection efficiency) and the ultimate limiting factor to the resolution is represented by the source size [7]. Hence decreasing the source size is a fundamental issue to achieve high resolution phase contrast imaging with a laboratory setup. Examples of phase contrast obtained with laboratory laser-based x-ray source have been reported [10]. Such source can provide a pulsed x-ray beam with good flux but the resolution, limited by the stability of the laser beam, was about 10  $\mu\text{m}$ . Much higher resolution has been reported using an x-ray source based on a Scanning Electron Microscope [11,12], creating an

extremely small source size. The latter examples are obtained using non-conventional x-ray sources. In this report we describe an alternative approach to high resolution imaging, based on a conventional source. We show the results obtained with a standard laboratory source equipped with a phase contrast microscope based on the x-ray waveguide (WG). The x-ray WG constitutes a reliable way to generate a small x-ray source. The described setup is compact, simple and inexpensive, and can be successfully applied to high resolution phase contrast imaging of low absorbing specimens.

## 2. X-ray WG microscope

A WG for x-rays has been demonstrated to provide a sub-micrometer beam whose size does not depend from the size of the primary source [13,14]. The principle of a WG has been extensively explained elsewhere [13–15]: a core material with index of refraction  $n_0$ , surrounded by a cladding material with index of refraction  $n_1 < n_0$  can act as a confining device for the radiation. Therefore if an electromagnetic wave is suitably coupled to the WG, it can be trapped in the core material and transmitted with low losses. In the x-ray region the core material could be simply air (or vacuum) and it can be sized down to sub-micron dimension.

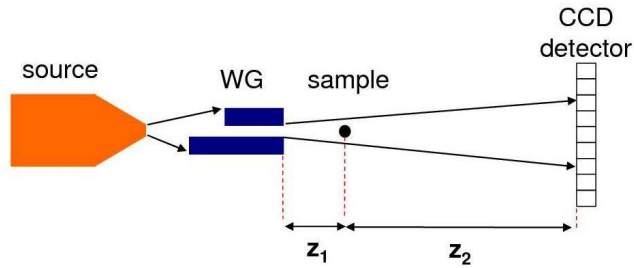


Fig. 1. Experimental setup for projection x-ray microscopy with WG.

The diffraction effect at the WG exit eventually produces a divergent beam that can be directed on a sample in projection geometry. In this configuration (see Fig. 1), indicating with  $z_1$  **the distance from the WG to the sample and with**  $z_2$  the distance sample – detector, a magnified image of the sample is projected onto the detector. The magnification factor is  $M = (z_1 + z_2) / z_1$ . In this way the WG acts as a sub-micron sized secondary source, improving both spatial resolution and coherence properties of the incident beam [16]. In projection geometry it can be shown [17] that an estimate for the resolution is:

$$r_t = \sqrt{\left( s \frac{z_2}{z_1 + z_2} \right)^2 + \left( PSF \frac{z_1}{z_1 + z_2} \right)^2} \quad (1)$$

where  $s$  and  $PSF$  are the Full Width at Half Maximum of the WG exit intensity distribution and of the detector Point Spread Function respectively. If  $s \ll PSF$ , as in the case of the WG, the best resolution is obtained for  $z_1 \ll z_2$ . On the other hand, large  $z_2$  means low flux density at the detector, and low  $z_1$  implies a limited field of view.

In the propagation-based phase contrast imaging the propagation distance plays a crucial role [7]. Three main imaging regimes are usually considered: near-field, Fresnel and Fraunhofer regimes. Being in one or another depends on the ratio  $r$  between the defocusing distance, defined as  $z_{def} = z_1 z_2 / (z_1 + z_2)$ , and the Fresnel distance  $f = d^2 / (4\lambda)$ , where  $d$  is the typical dimension of the illuminated sample features and  $\lambda$  is the wavelength. Our case corresponds to the near-field regime, where  $r \ll 1$  and the maximum contrast is obtained at

the sample edge discontinuity [7]. In the experiments reported here we used different planar asymmetric front-coupling WGs with vacuum core and Silicon claddings [15,18]. The length of the WG devices was 5 mm. The virtual source was then a line source and the magnification effect took place in one dimension only.

As for the coupling of the radiation into the WG and the transmission efficiency through the channel, a detailed treatment is given in [18]. Here we recall that the spatial acceptance, in asymmetric front coupling geometry, is given by  $2s$  and the angular acceptance is limited by  $2\theta_c$ , being  $\theta_c$  the critical angle for total reflection. The laboratory source was a microfocus NOVA 600 (Oxford Instruments) with Cu anode (wavelength  $\lambda = 0.154$  nm) and nominal source size  $w = 15$   $\mu\text{m}$ . In our experimental geometry the minimum allowable distance source-WG was  $L = 1$  cm. Therefore the angular acceptance of the WG was limited, in our case, by the geometry and can be estimated as  $\Delta\alpha = (w + 2s) / L \approx 1.5$  mrad. The transmission efficiency through the WG, following the calculation given in [18] has also been estimated close to unity, due to the relative large size of the gap  $s$  and the short length of the device.

Incidentally we note that the system provides also a broad energy filter for the incoming radiation. The WG works in total reflection conditions, thus the high energy *bremsstrahlung* from the source is not reflected and mostly absorbed by the cladding. The transmitted radiation is thus Cu K $\alpha$  ( $\Delta\lambda/\lambda \sim 10^{-3}$ ) with extremely low high-energy background. Finally we estimate the transverse coherence length  $l_c \approx \lambda L / w$  of the radiation at the WG entrance, which was of the order of 100 nm. We used two different WGs with gap size of about 200 nm and 300 nm respectively. Thus this configuration provided a partial coherent illumination at the WG entrance. The WG was not working as a fully coherent optical resonator, but it was closer to a capillary optics with submicron size [18]. Nevertheless the degree of coherence at the sample, because of the small dimension of the beam at the WG exit, was enough to show phase contrast effects.

### 3. Experimental results

In order to test the microscope and to evaluate the resolution limit and the contrast, we measured different objects: a Kevlar fiber nominally having a circular cross section with radius of 7  $\mu\text{m}$  (Fig. 2), different microfabricated gold test patterns constituted of three different sections with periodic structures (Fig. 3) and a human hair (Fig. 4).

In order to compare the measurements with a theoretical model, we performed numerical calculations based on the Fresnel-Kirchhoff integral [19], taking into account the actual resolution of the system estimated with Eq. (1). The size  $s$  of the WG secondary source was approximated by an effective Gaussian distribution [16].

The experimental set-up is sketched in Fig. 1. The sample stage, moveable along the longitudinal direction, allowed the geometrical magnification to be changed. We used a CCD detector with nominal pixel size of 12.3  $\mu\text{m}$  and measured  $PSF = 18$   $\mu\text{m}$ .

Figure 2 reports the experimental results of the Kevlar fiber, recorded at different distances  $z_1$ , while the total distance was kept constant:  $z_1 + z_2 = 420$  mm. Figure 2A shows, as an example, the normalized intensity distribution as recorded by the CCD detector, acquired with magnification  $M = 41$ . Only one edge of the fiber is visible across the field of view. Similar images were recorded at different magnification values. From these images we extracted the cross section intensities, reported in Fig. 2B–2D. They are obtained by integration over the longitudinal direction of the fiber, of the 2-D images. The acquisition time was 150 s for all exposures. The measured intensity (red dots) was normalized with respect to the incident beam, background corrected and superimposed over calculated profile (black solid line) for comparison. The fiber was modeled as a Kevlar cylinder with  $\delta = 4.84 \times 10^{-6}$  and  $\beta = 9.74 \times 10^{-9}$ . In Fig. 2C–2E the two fringes at the edges have a different visibility. This can be ascribed to the non-perfect alignment of the fiber in the beam and to any possible deviation of the fiber from a cylindrical shape. Nevertheless, the agreement between experimental results and theoretical simulations is qualitatively very good.

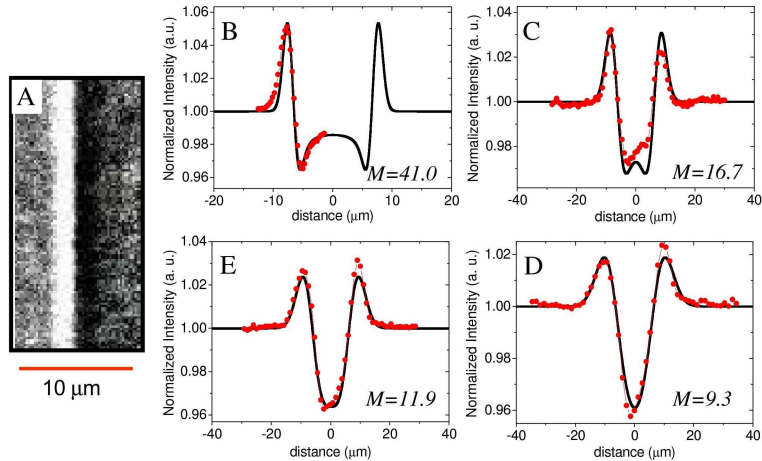


Fig. 2. Experimental results about the Kevlar fiber. A) Measured intensity with geometrical magnification  $M = 41$ . The measurement shows the phase contrast at the interface air-fiber. The fiber is on the right. B-E) Cross section intensities, integrated along the longitudinal direction of the fiber for different magnifications (red dots) superimposed over the corresponding analytical simulation (black solid line).

The second set of measurements is relative to the gold test pattern. It was grown on a  $\text{Si}_3\text{N}_4$  membrane. The thickness of the gold structure was 600 nm. We imaged gold stripes of different widths (2.2  $\mu\text{m}$ , 1.1  $\mu\text{m}$  and 0.64  $\mu\text{m}$ ) and separations (1.8  $\mu\text{m}$ , 0.9  $\mu\text{m}$  and 0.38  $\mu\text{m}$ ), see Scanning Electron Micrographs of the three structures in Fig. 3A–3C. We used in this case a WG with 300 nm gap size. The measurements are reported in Fig. 3D–3F. All images were acquired with  $z_1 = 2$  mm and  $z_1 + z_2 = 450$  mm, therefore with a constant magnification  $M = 225$ . The exposure time was 60 s. The normalized intensities, integrated in the vertical direction, are reported and superimposed to the analytic simulations in Fig. 3G–3I.

Regarding the expected resolution, the source and detector terms in Eq. (1) are respectively 0.3  $\mu\text{m}$  and 0.08  $\mu\text{m}$ , giving a value  $r_t = 0.31$   $\mu\text{m}$ . This value has been used in the theoretical calculations reported in Fig. 3G–3I. The agreement between calculations and measurements is good. WG and samples imperfections (not accounted in the theoretical calculations) are responsible for a non perfect agreement. Indeed the system shows a spatial resolution of 300 nm, useful to distinguish the closest structures of Fig. 3C, 3F.

In order to show an example of the possible applications of the phase-contrast microscope described before, we present here some images obtained on a human hair. Figure 4A shows the image obtained with a standard Cu sealed tube (line focus, effective source size: 40  $\mu\text{m} \times 8$  mm), where only the absorption contrast is visible and the spatial resolution is quite poor. Figure 4B shows the same sample, but with a vacuum-gap WG interposed between the same standard x-ray source used in Fig. 4A, and the sample. The WG was at a distance  $L = 9$  cm from the source, oriented with the gap parallel to the smallest source dimension. The sample was at a distance  $z_1 = 3.3$  cm from the WG exit, and the detector at a distance  $z_2 = 27.7$  cm from the sample. The magnification factor was therefore  $M = 9.4$  and the resolution, from Eq. (1), was  $r_t \sim 2$   $\mu\text{m}$ . In this case, the small size of the WG exit gap and the optimized geometry produce a clear phase contrast fringe at the interface air-hair. The increase in contrast and resolution is evident in the second picture (Fig. 4B), from which useful structural properties of the hair could possibly be derived. Further studies in this direction are in progress.

#### 4. Conclusions

In conclusion, we have demonstrated in this report that the X-ray WG- based microscope can provide phase contrast images at spatial resolution of few hundred nanometers, both from

inorganic low-Z samples such as a fiber, from high-Z nanopatterned samples, and from biological samples, using either microfocus or standard x-ray laboratory sources.

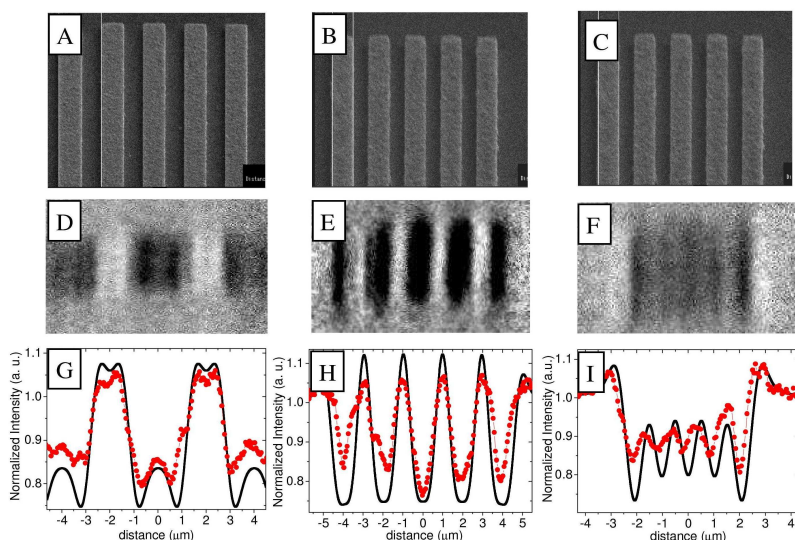


Fig. 3. A-C) SEM images of the structures made by five gold stripes 600 nm thick with the significant distances used to test the resolution and D-F) the respective experimental images recorded by the CCD based detector. The acquisition time was 60s. The magnification effect takes place in the horizontal direction only. The black regions correspond to higher absorption (gold bars) although modulated by interference fringes because of the propagation. In G-I) the normalized intensity (red dots), integrated in vertical direction of D-F) respectively is reported. The experimental curves are superimposed on the analytical simulations (black solid line), considering a spatial resolution of 300 nm.

The WGs used in this study were relatively simple and cheap, and they didn't require particularly complex experimental set-ups. In this work we used planar WGs, allowing only 1-D studies. However, as demonstrated in previous studies with synchrotron radiation [20], many crucial problems in biology and material science require high resolution analysis only in one-dimension. The image of the human hair shown here is just an example of a biological sample.

Extension to 2-D imaging is as well in progress. The expected exposure time is proportional to the resolution increase (in 1-D), i.e. we expect an increase a factor 10 moving from 1-D to 2D high resolution imaging, for a given Signal-to-Noise ratio. Two crossed WGs were recently used to provide a point virtual source for Coherent X-ray Diffraction Imaging (CXDI) experiments with a curved wave front [21]. 2-D WGs have been also fabricated [22] and their optimization for laboratory x-ray sources is in progress.

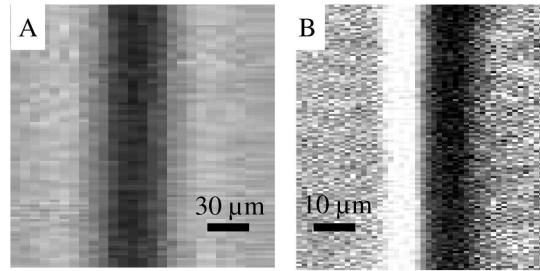


Fig. 4. Two different images of the same human hair (diameter  $\sim 67 \mu\text{m}$ ). The image in A) was taken without the WG. In this case we see the whole hair cross section but with poor resolution ( $r_i \approx 25 \mu\text{m}$ ) and poor contrast. In B) we look at the air-hair interface only, using an x-ray WG with 200 nm vacuum gap. The hair is on the right hand side of the picture. In analogy with Fig. 2A a good visibility phase contrast fringe is visible. The improvement in contrast and resolution ( $r_i \approx 2 \mu\text{m}$ ) is noticeable.

### Acknowledgements

The project SPARX and PRIN 2007ZT39FN\_003 are acknowledged for partial financial support. The COST action MP6010 is also acknowledged.